AIAA JOURNAL
Vol. 45, No. 12, December 2007

Lift Enhancement over Flexible Nonslender Delta Wings

G. Taylor,* Z. Wang,† E. Vardaki,* and I. Gursul‡
University of Bath, Bath, England BA2 7AY United Kingdom

DOI: 10.2514/1.31308

Unsteady aerodynamics of flexible nonslender delta wings is investigated in an experimental study using various techniques. Dramatic fluid/structure interactions emerge with increasing wing flexibility and result in substantial lift enhancement in the poststall region. This recently discovered phenomenon appears to be a feature of nonslender wings. Self-excited antisymmetric vibrations of the wing promote reattachment of the shear layer, which results in the lift enhancement. These self-excited vibrations are not observed for a half-model. The Strouhal number of the dominant frequency of the structural vibration is on the order of unity for all nonslender wings, which also corresponds to the frequency of the shear-layer instabilities for the rigid wing. Velocity measurements demonstrate the striking difference between the flows over the flexible and rigid wings in the poststall region. The effect of flexibility is to promote the reattachment of the shear layer near or downstream of the apex, depending on the incidence. There are substantial effects on the vortical flow with increasing wing flexibility, which might lead to the axial flow developing within the reattached region. The time-averaged vorticity flux increases due to the oscillating leading edge, which leads to increased circulation.

Nomenclature

b	=	span
C_L	=	lift coefficient
Coh	=	coherence of velocity fluctuations
c	=	chord length
E	=	elastic modulus
E_u	=	spectral density of velocity fluctuations
f	=	frequency
fc/U_∞	=	dimensionless frequency
q	=	freestream dynamic pressure
Re	=	Reynolds number based on the chord length
S	=	wing reference area
Sr	=	Strouhal number, fc/U_∞
s	=	semispan
t	=	wing thickness
U	=	velocity vector
U_∞	=	freestream velocity
u	=	streamwise or chordwise velocity
v	=	spanwise component of velocity
x	=	chordwise distance
y	=	spanwise distance
z	=	normal (to the wing surface) distance
α	=	angle of attack
δ	=	wingtip vertical deflection under load
λ_s	=	spanwise bending stiffness normalized by freestream dynamic pressure, $12(1-\nu^2)\rho_\infty U_\infty^2 s^3/Et^3$
Λ	=	leading-edge sweep angle
ν	=	Poisson's ratio
ρ	=	density

I. Introduction

RECENT interest in unmanned air vehicles has resulted in a need for a better understanding of flow physics and also for effective flow control strategies. Low-sweep wings with sweep angles in the range of 35 to 55 deg are often used in current and future concepts of unmanned combat air vehicles (UCAVs) and micro air vehicles (MAVs). All these configurations exhibit separated and vortex-dominated flows, in particular, at low Reynolds numbers [1]. Vortical flow over nonslender delta wings has recently become a topic of increased interest in the literature. Although the flow topology over more slender wings, typically $\Lambda \geq 65$ deg, has been extensively studied and is now reasonably well understood [2–5], the flow over lower-sweep wings has only recently attracted more attention [6,7]. Vortical flows develop at very low angles of attack and form close to the wing surface. This results in strong interactions with the upper-surface boundary layer. Although a slender wing typically exhibits a coherent primary vortex generated by the rollup of the shear layer separating from each leading edge, recent computational and experimental studies have demonstrated that a dual primary vortex structure exists over nonslender wings at low incidence. This vortex structure is a direct result of the proximity of the vortex formation to the wing surface and the corresponding interaction with the surface boundary layer. The vortices generated over low-sweep delta wings undergo breakdown at very low incidences [8]; for a 50-deg wing, the breakdown has been observed over the upstream half of the wing at an incidence of just 2.5 deg. Vortex breakdown is observed to be much less abrupt compared with breakdown over slender wings. Compared with more slender planforms, nonslender wings have lower maximum lift coefficient and also lower stall angle [9–11]. According to Polhamus's leading-edge suction analogy [12], the vortex lift contribution becomes a smaller portion of the total lift as the sweep angle decreases. Also, there is no obvious correlation between the onset of vortex breakdown over nonslender wings and the change of the lift coefficient [11].

A unique feature of nonslender vortices is that primary attachment occurs outboard of the symmetry plane even when vortex breakdown is close to the apex. With increasing incidence, this attachment line moves inboard toward the wing centerline. Just before stall, substantial buffeting is associated with the attachment region. With further increase of angle of attack, reattachment is no longer observed, corresponding to stall of the wing. Active and passive control of reattachment may be beneficial for lift enhancement in the poststall region.

The next generation of unmanned flight vehicles will be highly flexible, will have lower structural-weight-to-takeoff-weight ratios, and will be capable of performing extreme maneuvers at high gravity. Hence, wing flexibility becomes an important issue. The coupling of unsteady, separated, and vortical flows with flexible

Received 3 April 2007; revision received 10 July 2007; accepted for publication 12 July 2007.

*Research Officer, Department of Mechanical Engineering.
†Research Councils United Kingdom Academic Fellow, Department of Mechanical Engineering.
‡Professor, Department of Mechanical Engineering. Associate Fellow AIAA.

wings may be significant. This fluid–structure interaction is expected to be more pronounced for nonslender wings. Also, wing vibrations mean that the oscillating leading edge is an unsteady source of vorticity. Although the flows over nonslender wings have become a more popular topic in the literature over recent years, there have been few investigations on the effect of flexibility for delta wings. Studies of a slightly flexible wing of 60-deg leading-edge sweep have been performed both experimentally [13] and computationally [14]. For a wing of $t/c = 0.44\%$ and a Reynolds number of $Re = 9.6 \times 10^5$, large buffeting was observed in the region just before the stall. Spectral analysis of the wingtip acceleration showed that the unsteady loading occurred in the second antisymmetric mode. Computational simulations confirmed that the spectra of instantaneous pressure fluctuations contained broadband peaks centered around the second and third modes. For this moderately swept wing, vortex breakdown is the main source of unsteadiness and wing buffeting. The dominance of the antisymmetric mode suggests that the antisymmetric streamwise motion of the vortex breakdown location reported previously may also be coupling with the structural motion in this situation. Only recently, the effects of flexibility have been studied for a nonslender delta wing. Studies of a 50-deg wing of thickness $t/c = 0.65\%$ at a Reynolds number of $Re = 6.6 \times 10^5$ have also shown significant levels of buffet [8] around the stall angle. It was shown that the maximum buffeting occurs near $\alpha = 20$ deg, for which vortex breakdown occurs at the apex and there is no streamwise vortex with axial flow. However, shear-layer reattachment near the wing centerline produces large unsteadiness and wing buffeting.

A recent study has documented a particularly interesting feature of nonslender wings of sufficient flexibility [15]. It was shown that for a wing of thickness $t/c = 0.32\%$ at a Reynolds number $Re = 6.2 \times 10^5$, a region of significant lift enhancement exists in the range of incidences immediately following the stall. This lift enhancement was associated with self-excited wing vibrations in the poststall region. Subsequent work was presented in several conference papers [16–18]. Most recently, we have conducted further experiments. The purpose of this paper is to summarize our studies and understanding of this phenomenon. Various experimental methods were used to study the unsteady aerodynamics of flexible nonslender delta wings. These include force measurements, particle image velocimetry (PIV) and laser Doppler velocimetry (LDV) measurements, flow visualization, hot-wire measurements, and deformation measurements.

II. Experimental Methods

A. Facilities and Models

Wind-tunnel experiments were conducted in the high-speed working section of the 7×5 ft (2.1×1.5 m) closed-circuit facility at the University of Bath. Models were supported using the high-incidence mechanism shown in Fig. 1. Experiments were conducted at a freestream velocity of $U_\infty = 31$ m/s. Models of varying leading-edge sweep and thickness were tested. Each model was a planar delta wing with a pressure surface leading-edge bevel of 45 deg and a square trailing edge. Figure 2 shows a schematic of the

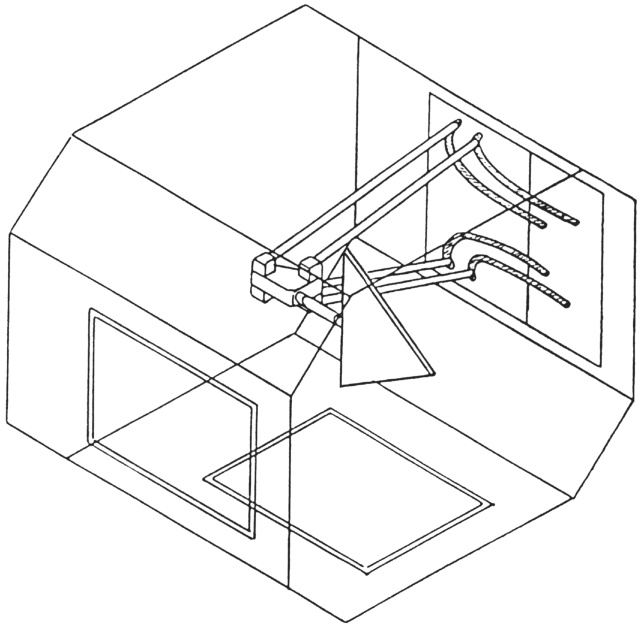

Fig. 1 Schematic of the working section and high-incidence mechanism of the 7 × 5 ft wind tunnel.

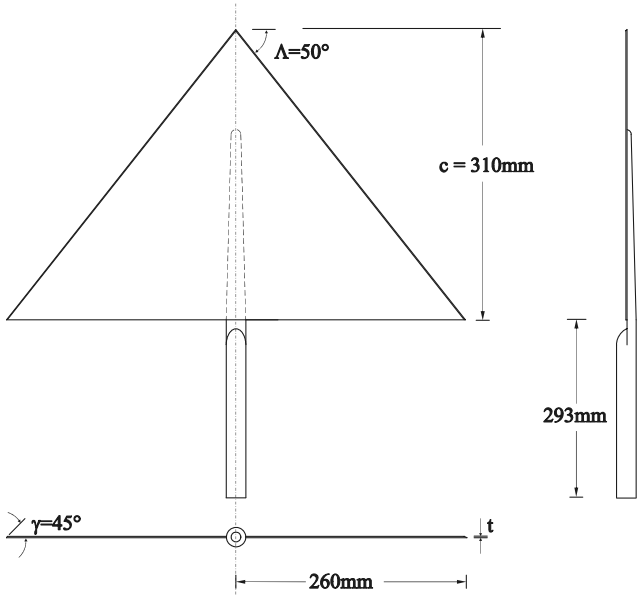

Fig. 2 Principle model dimensions of the flexible wing with a leading-edge sweep of $\Lambda = 50$ deg.

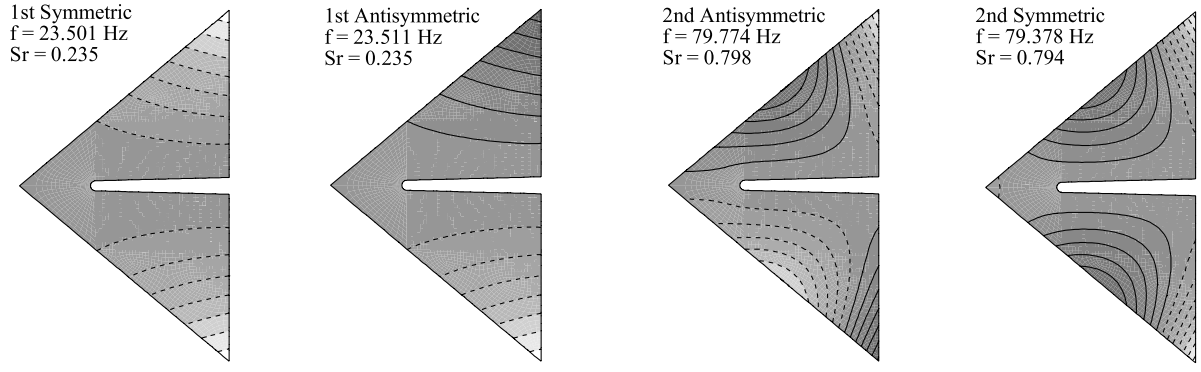

Fig. 3 Finite element modal solutions for the flexible wing ($t/c = 0.32\%$) for $\Lambda = 50$ deg.

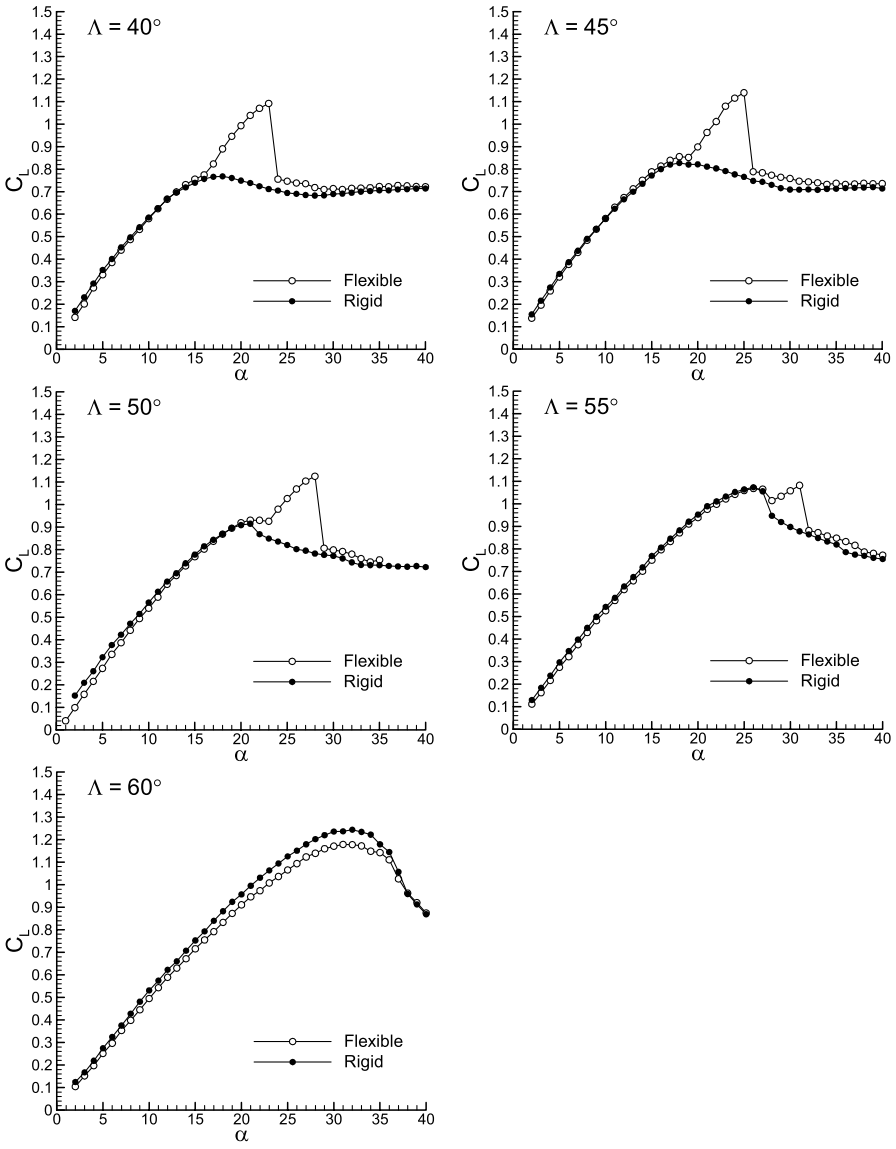

Fig. 4 Variation of the time-averaged lift coefficient with incidence for all wings tested.

wing with a 50-deg leading-edge sweep; in addition to this, wings of 40-, 45-, 55-, and 60-deg sweeps were tested. Each model had a semispan of $s = 0.260$ m such that the spanwise flexural characteristics of the thin wings remained consistent between the models. Chord lengths c in the range of 0.218–0.450 m were used, resulting in chord Reynolds numbers in the range of 440,000–900,000. Maximum blockage for the wind tunnel was approximately 2.3% for the 60-deg wing at $\alpha = 50$ deg. Each model was made from aluminum alloy 1050A, which has the following material properties: $\rho = 2700$ kg/m^3, $E = 69$ GPa, and $\nu = 0.3$. Models of thickness 1 mm ($t/s = 0.38\%$) and 5 mm ($t/s = 1.92\%$) were tested. The 1-mm wing was designed for high flexibility and achieved significant out-of-plane deflections as documented in [15], whereas the 5-mm wing was rigid. The parameter $\lambda_s = 12(1 - \nu^2)\rho_\infty U_\infty^2 s^3/Et^3$, the reciprocal of the spanwise bending stiffness of the wing normalized by the freestream dynamic pressure, was used to give an indication of the relative flexibility of the wings, whereby a higher value of λ_s corresponds to a more flexible wing. The preceding conditions resulted in a nondimensional spanwise bending stiffness, $\lambda_s = 3.1$ for the 1-mm wing of all sweep angles, compared with a value of $\lambda_s = 0.025$ for the rigid wings.

ANSYS finite element software was used to predict the structural modes of vibration of the 1-mm flexible wings before experimental testing. The finite element model used 2844 SHELL63 elastic shell elements and represented a full geometric model to allow both symmetric and antisymmetric modes of vibration to be calculated. The presence of the support was modeled by removing elements from the region affected by the support and by applying a fully clamped boundary condition to the nodes that would be in contact with the support. Although significant time-averaged deflections were observed, a planar model was analyzed for simplicity. Material properties applied to the model were based on the properties of the aluminum alloy 1050A. Figure 3 shows the first two mode shapes for a wing of 1-mm thickness and $\Lambda = 50$ deg with uniform material properties. The fundamental mode was predicted at $f = 23.501$ Hz and comprised a simple symmetric bending of the wingtips. At a slightly higher frequency, $f = 23.511$ Hz, an antisymmetric version

Table 1 Maximum lift coefficient for rigid and flexible wings as well as lift increment and stall delay for varying sweep angles. Increment in maximum lift coefficient achieved by the flexible wing is compared with 1) the maximum lift coefficient of the rigid wing and 2) the lift coefficient of the rigid wing at the stall angle of the flexible wing

	$C_{L\max}$		$\Delta C_{L\max}$		
Λ	Rigid	Flexible	1	2	$\Delta\alpha_{\text{stall}}$
40	0.77	1.09	42%	53%	7 deg
45	0.83	1.14	38%	49%	6 deg
50	0.92	1.13	23%	45%	5 deg
55	1.07	1.08	1%	23%	3 deg
60	1.24	1.18	−5%	−5%	0 deg

of the fundamental mode was observed, which will be referred to as the first antisymmetric mode. The second antisymmetric mode occurred at $f = 79.774$ Hz and was accompanied by the second symmetric mode at $f = 81.143$ Hz. The third symmetric mode involved an out-of-plane bending of the apex at $f = 118.39$ Hz, and the third antisymmetric occurred at a slightly higher frequency of $f = 122.05$ Hz. Mode shapes for other sweep angles were similar.

In addition to the extensive wind-tunnel experiments, complementary experiments were conducted in a water-tunnel facility located at the University of Bath. The tunnel is an Eidetics Model 1520 free-surface water tunnel, which has a $0.381 \times 0.508 \times 1.524$ m test section and can achieve speeds up to 0.45 m/s through a closed-circuit continuous-flow system. The tunnel has four viewing windows: three surrounding the working section and one downstream, allowing axial viewing. The height of the test section above the floor is adequate to allow flow visualization viewing from below as well as from the sides. The tunnel also incorporates a dye system with six available dye tubes to enable flow visualization with different colors.

Water-tunnel experiments were conducted with rigid and flexible delta wings with 50-deg sweep angles. The rigid wing was made of aluminum and had a 45-deg bevel on the leading and trailing edges on the pressure surface. The model had a chord length of $c = 89$ mm and a thickness of $t = 2$ mm, giving a thickness-to-chord ratio of $t/c = 2.25\%$. The Reynolds number, based on the chord length, was $Re = 26,000$ for all the experiments. Four different flexible wings were tested with thicknesses of 0.1905, 0.254, 0.381, and 0.508 mm, respectively. The former two wings were made out of polyester and the latter two out of polypropylene. Here, the parameter λ_s, which is the spanwise bending stiffness normalized by freestream dynamic pressure, takes the values of $\lambda_s = 0, 2.4, 5.6, 9.0$, and 21.3, which is a much wider range of flexibility compared with the wind-tunnel experiments. The wings were mounted upside down on the tunnel using a sting projecting from the rear of the model.

B. Techniques

Force-balance measurements were undertaken using a six-component strain-gauged internal balance. Forces were normalized by qS and moments were normalized by qSc, where q is the freestream dynamic pressure, S is the wing reference area, and c is the root chord. The output from the force balance was recorded using a desktop PC with a 12-bit A/D data acquisition card. Time-averaged force/moment coefficients were obtained in addition to the root mean square (rms) quantities after filtering of the voltage signal above 1 kHz (corresponding to $Sr \approx 10$). Measurement uncertainty for the lift coefficient was estimated to be 2%. Wingtip displacements were measured using a high-speed Kodak digital camera with a resolution of 512×240 pixels and a capture rate of 500 frames per second. Tip displacements were measured from the resulting images and calibrated to give measurements in SI units. Buffet response was measured by mounting Entran EGA miniature accelerometers with a mass of approximately 0.5 g on each tip of the flexible wings. Signals from the accelerometers were recorded using a desktop PC with a 12-bit A/D data acquisition card. Signals were recorded for a period of 5 s at a sampling frequency of 1000 Hz, resulting in a record spanning over 250 c/U_∞.

Surface flow visualizations were achieved using lengths of thin fluorescent thread (Glo-Brite Fluorescents) taped to the wing. The threads were placed with a density of around 2.5 threads per centimeter, and each thread was approximately 20 mm long. Both surface flow and wingtip visualizations were captured using a digital video camera with a resolution of just under two million pixels.

Quantitative flow measurements were undertaken using digital particle image velocimetry (DPIV). Two different PIV systems were used. Most of the measurements presented in this study were taken using a TSI Solo DPIV system. The system incorporates a pair of pulsed mini Nd:YAG lasers with a maximum energy of 120 mJ per pulse, which was used to illuminate the plane of interest. The maximum field of view attainable is approximately 300 by 300 mm. Images were captured using an eight-bit TSI PowerView 4M CCD digital camera with a resolution of 2048×2048 pixels and a maximum capture rate of 7.5 frames per second, producing 3.75 frames in cross-correlation. For these measurements, the flow was seeded using a commercially available smoke generator. For all the crossflow measurements, 2000 instantaneous images were captured. A combination of cylindrical and spherical lenses was used to generate the required light sheet. For crossflow measurements, the

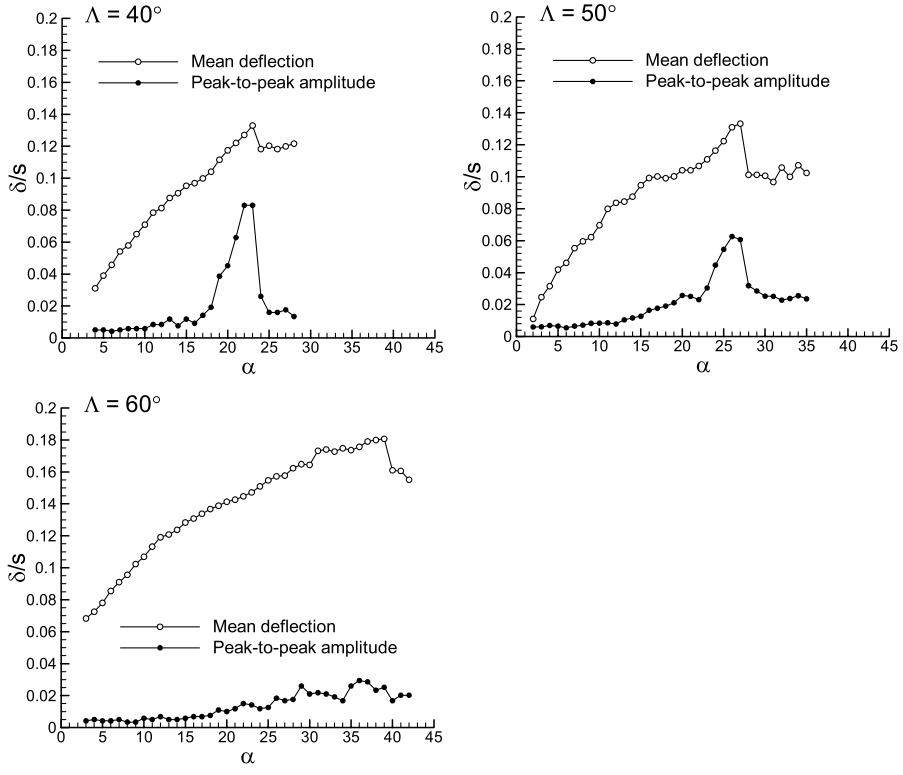

Fig. 5 Variation of the time-averaged and fluctuation amplitudes of wingtip deflections with incidence.

laser light sheet was placed normal to the freestream. In addition, the light sheet was placed parallel and close to the wing surface to reveal the near-surface flow pattern. In practice, the distance from the wing surface was prescribed by the need to reduce surface reflections and was in most cases around 1 mm (0.3% of the chord length). For the flexible wing, the deformation of the wingtips interfered with this measurement plane, therefore the light sheet was placed at an angle of approximately 5 deg with respect to the wing. The commercial software package TSI Insight version 6.0 and a fast Fourier transform (FFT) cross-correlation algorithm were used to analyze the images, with an interrogation window size of 64 by 64 pixels, and to produce velocity vectors for further processing. The effective grid size was 2% of the local semispan s in crossflow measurements and around 0.9% of the chord length in measurements in a plane near the wing surface. The measurement uncertainty for the velocity is estimated as 2%.

The second system, with which measurements in streamwise planes were taken, was a high-frame-rate DPIV. This system provides both temporal and spatial information of the flowfield. Illumination of the desired plane was achieved using a New Wave Pegasus Nd:YLF double-pulse high-speed laser with a maximum energy of 10 mJ per pulse. The laser was placed parallel to the freestream velocity. The images were captured using a TSI PowerView HS-3000 high-speed CMOS camera. A TSI LaserPulse synchronizer unit was used to link the camera and the laser to enable the accurate capture for a two-frame cross-correlation analysis. For the streamwise results presented, the system was operated at 3 kHz, giving an area of resolution of 1024 by 1024 pixels. This allowed the capture of the velocity field at 1.5 kHz, and 300 images were captured for each of the streamwise station measured for both the rigid and flexible wings. A TSI model 9307-6 multijet atomizer was used, producing oil droplets to seed the flow. The atomizer worked best using olive oil and the mean size of the droplets was 1μ. The commercial software TSI Insight3G and a FFT cross-correlation algorithm were used for the analysis of the results obtained. The size of the interrogation window was 32 by 32 pixels. The grid size varied from 0.8 to 1%c in these measurements.

LDV measurements were undertaken using a 300-mW air-cooled argon–ion laser and TSI burst correlator unit. The data rate was in the range of 200 to 300 Hz, with a burst efficiency of approximately 50%, and a total of 5000 data points were recorded for each test, giving a sample period of well over 100 c/U_∞. Measurements of the chordwise velocity were taken in the crossflow plane at $x/c = 0.4$ and 0.7. Single traverses vertically above the centerline were also taken at a higher resolution, and the resulting velocity profiles for the rigid and flexible wings were compared.

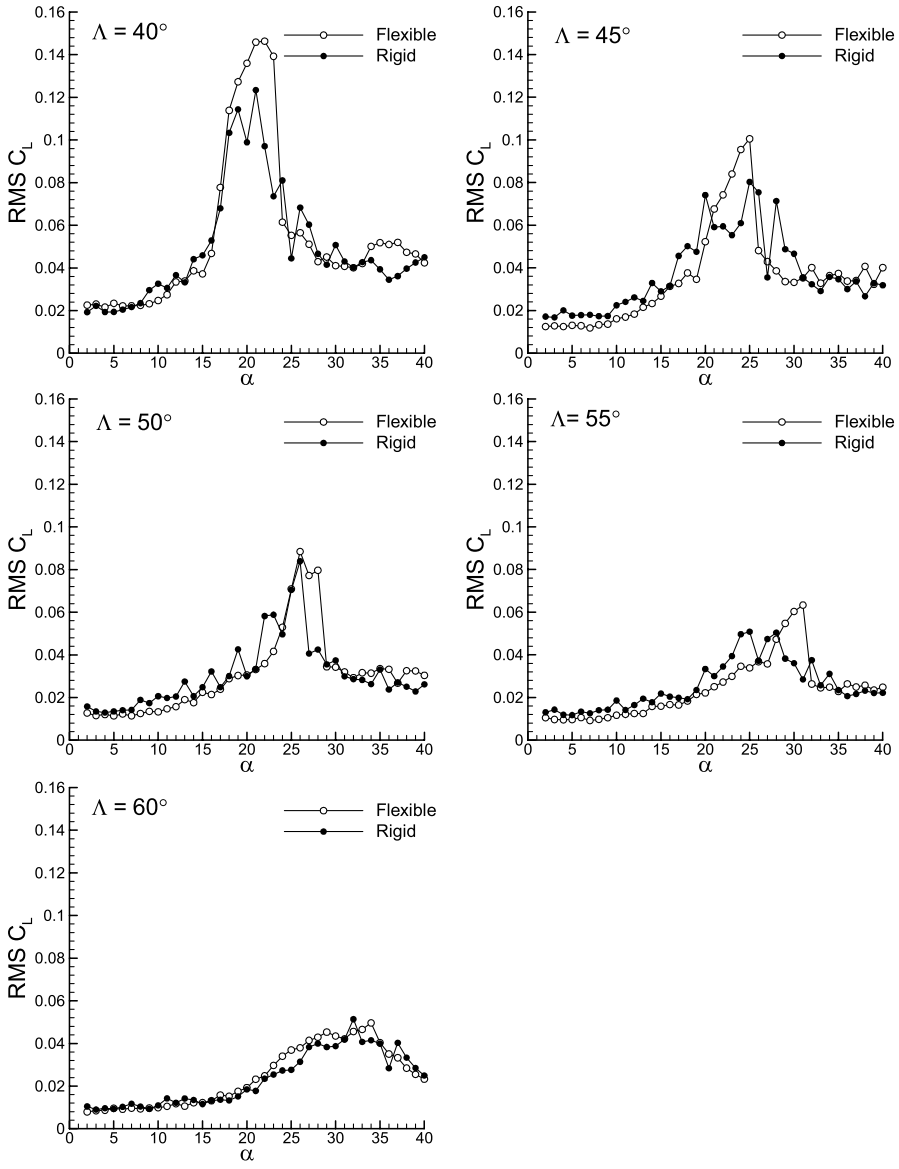

Fig. 6 Variation of the rms lift coefficient with incidence.

Hot-wire measurements were conducted for spectral analysis of unsteady flow features. These measurements were taken with a single hot-wire probe and also with two hot-wire probes for simultaneous two-point measurements.

In the water-tunnel experiments, visualization of the vortical flow was achieved using food coloring dye diluted 1:4 with water. A digital video camera with a capture rate of 25 frames per second and a resolution of 570,000 pixels was used to capture images from the dye flow visualization and was interfaced to a desktop computer via the commercial software package Pinnacle Studio DV, enabling real-time viewing of the wing and the capture of camera images and video recordings. For PIV measurements in the water tunnel, the flow was seeded with commercially available hollow glass particles of a mean diameter of 4 μm, and the PIV camera was placed near the downstream viewing window. To illuminate the desired planes, the laser system was placed underneath the test section of the water tunnel. The same PIV system with the 120-mJ/pulse laser was used in these measurements. The effective grid size was 2% of the local semispan s in these crossflow measurements. In these experiments, 30 images were used for time-averaging.

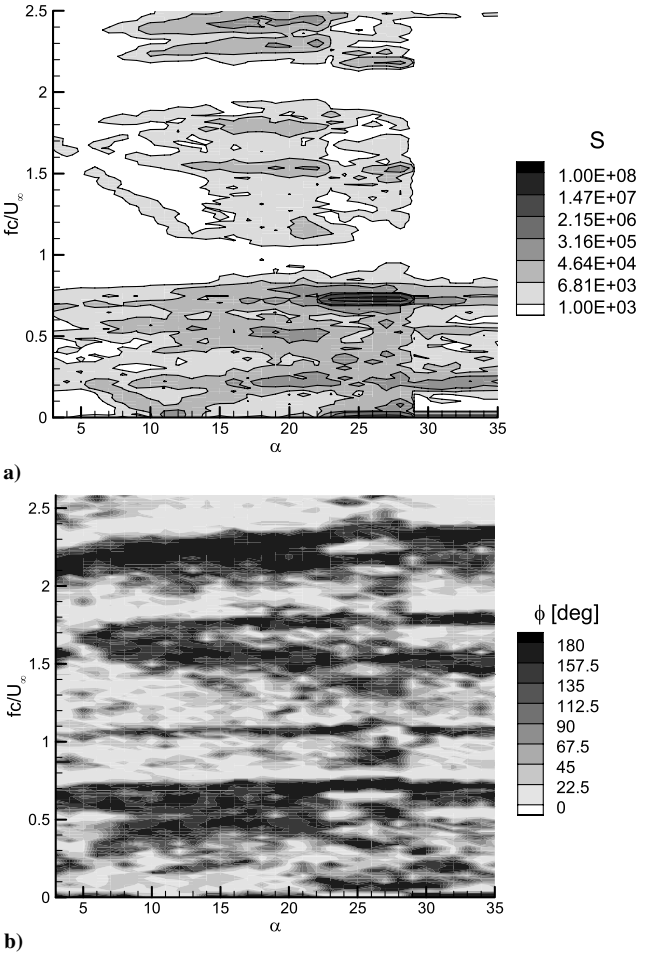

Fig. 7 Variation of a) cross-spectral amplitude and b) phase angle of the cross spectra between the two wingtip accelerations; the scale for the amplitude is logarithmic.

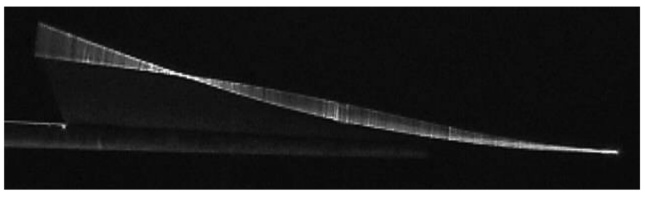

Fig. 8 Visualization of leading-edge deformation for 1-mm wing at $\Lambda = 27$ deg.

III. Results

A. Lift Enhancement on Flexible Wings

Figure 4 compares the variation of lift coefficient with incidence for the flexible and rigid wings of all sweep angles tested. The results show that the lift-enhancement phenomenon [15] is not limited to wings of 50-deg leading-edge sweep; rather, the effect of flexibility was to result in a region of enhanced lift for all wings except the 60-deg wing. Note that the stall for the flexible wings is very sudden, and the data shown in this figure were obtained by increasing the angle of attack. For decreasing angle of attack, there is slight hysteresis [15] around the stall angle of the flexible wings, which is typical of

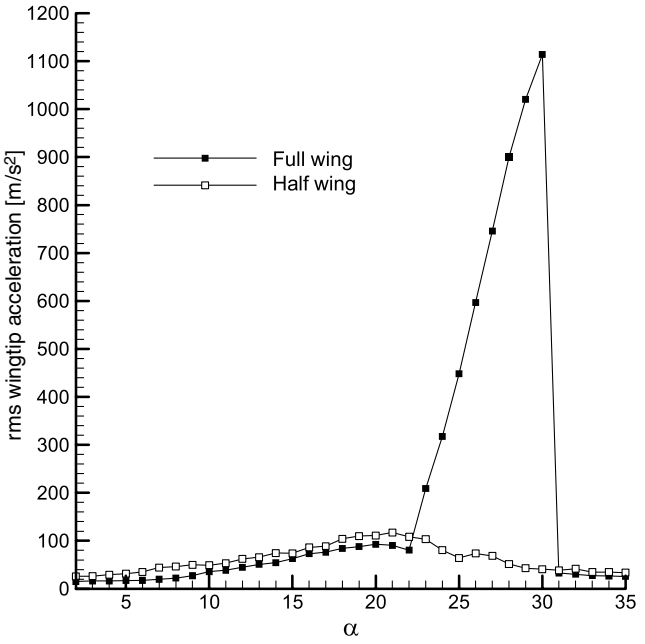

Fig. 9 Variation of rms wingtip acceleration for the 50-deg half-wing model and the full-wing model.

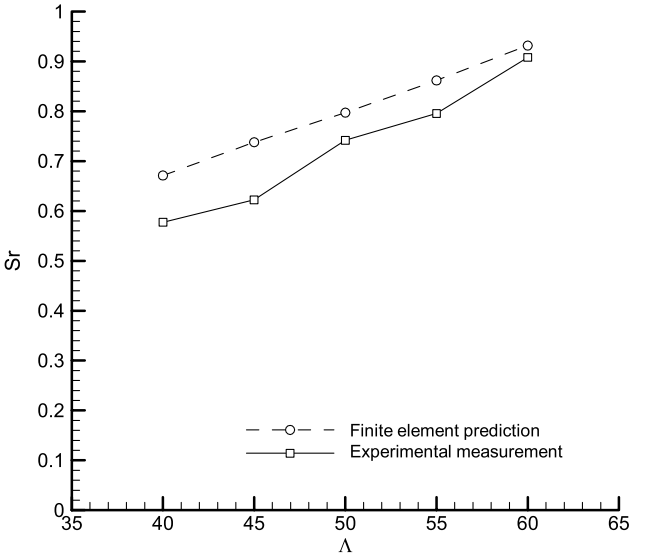

Fig. 10 Comparison of Strouhal number of second antisymmetric mode predicted by the finite element model with measured dominant frequency of wing vibrations.

separating and reattaching flows. The magnitude and extent of the lift-enhancement region was a function of sweep angle, with the greatest enhancement being observed over the wing of lowest sweep. This is further demonstrated in Table 1, which lists some statistics regarding the lift curves shown in Fig. 4. In this table, $\Delta C_{L\,\max}$ represents the increment in maximum lift coefficient achieved by the flexible wing compared with 1) $C_{L\,\max}$ of the rigid wing and 2) C_L of the rigid wing at α_{stall} of the flexible wing.

The 40-deg wing improved the maximum lift coefficient by over 40%, and at the point of stall of the flexible wing, lift coefficient was enhanced by over 50%. As sweep angle was increased, the magnitude of the lift enhancement reduced, with the overall maximum lift coefficient of the 55-deg wing increased by just 1%, whereas the 60-deg wing experienced an overall reduction in lift. Similarly, for the 40-deg wing, a delay in the onset of stall of 7 deg was achieved by the flexible wing, whereas no delay in stall was achieved for the 60-deg wing. For all the wings, the nose-down pitching moment measured about the apex (not shown here) underwent a similar magnitude increase in the lift-enhancement region. Because the variation of the pitching moment is very similar to that of the lift force [15], it will not be discussed any further here. The variation of the drag coefficient is also similar to that of the lift coefficient, as expected for the thin wings tested. Time-averaged drag also increases in the poststall region, resulting in no noticeable change in the lift/drag ratio [19].

Because no lift enhancement was observed for the largest sweep angle $\Lambda = 60$ deg, this phenomenon appears to be limited to the flexible low-sweep wings. On slender wings, reattachment occurs at the centerline at high incidences. A unique feature of the flow structure on nonslender wings is that the vortex and primary attachment zone are located further outboard from the wing centerline. This characteristic may be responsible for the increased impact of wing flexibility on the aerodynamic loading.

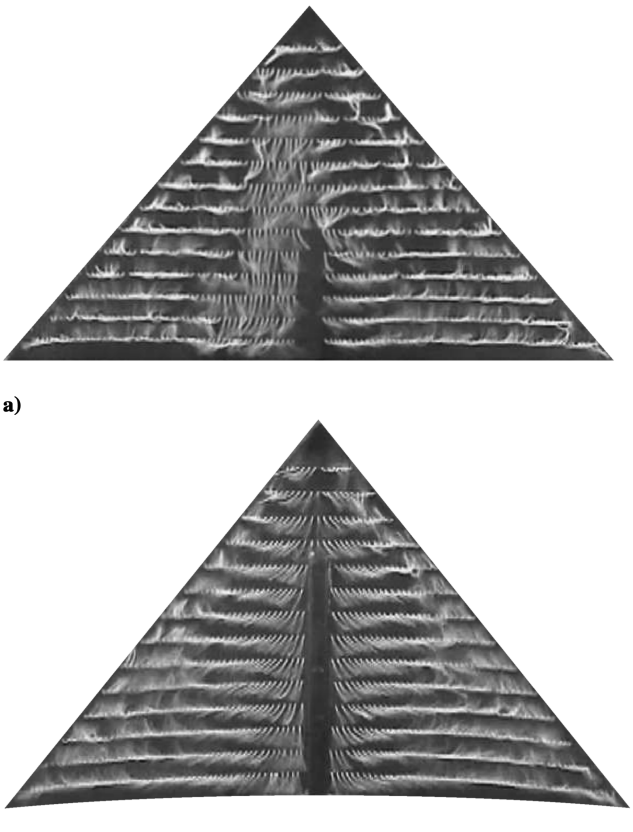

Fig. 11 Tuft visualizations showing surface flow patterns at $\alpha = 27$ deg for the a) rigid wing and b) flexible wing.

Because of the degree of flexibility employed in these experiments, considerable time-averaged and fluctuating displacements were observed. For the wings of 40-, 50-, and 60-deg sweeps, the variation of wingtip displacement with incidence is shown in Fig. 5. For the 40- and 50-deg wings, the lift-enhancement region was accompanied by an increase in both the amplitude and, to a lesser extent, mean (time-averaged) tip deflection. For the 60-deg wing, which did not experience an increase in lift, no such discontinuity in the displacement curves was observed. In fact, it is clear that the 60-deg wing experiences much less buffet than the lower-sweep wings, although the peak mean deflection is greater. Although the wings were designed to have identical values of λ_s and therefore equivalent bending stiffness, the chord lengths of the wings are not equal, resulting in a lower thickness-to-chord ratio for the 60-deg wing, and this probably accounts for the greater mean deflection for this wing. This result confirms that mean deflection alone does not cause lift enhancement. In earlier stages of this research [15], a rigid wing with 50-deg sweep angle was given a spanwise dihedral camber of a form such that its cross section approximately corresponded to the time-averaged deformation of the flexible wing. The results showed that there was no lift enhancement due to the static spanwise camber. All

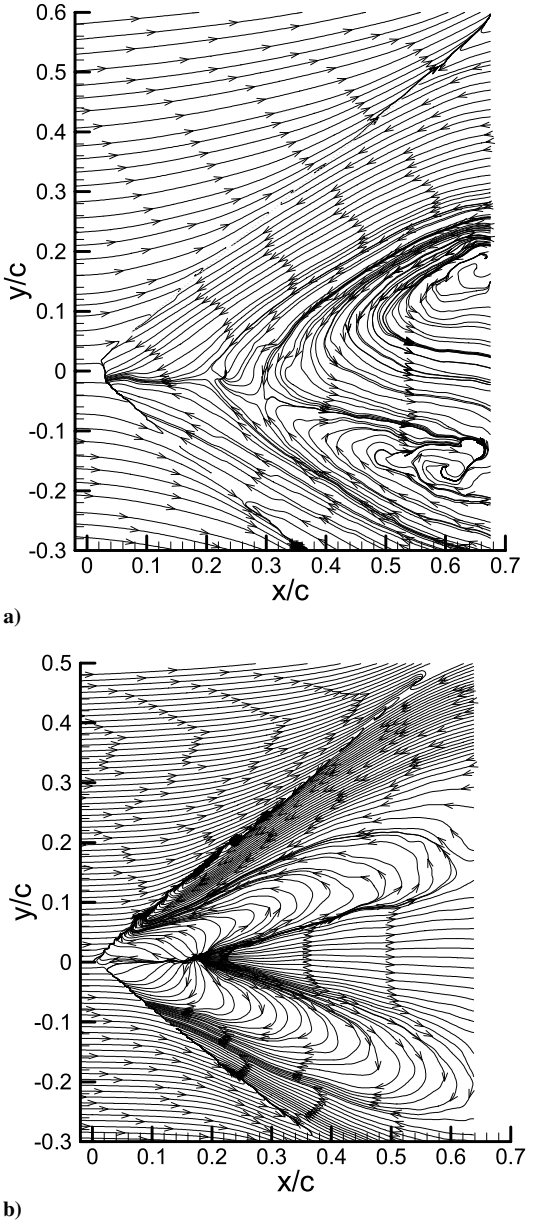

Fig. 12 Near-surface time-averaged streamlines at $\alpha = 27$ deg for a) rigid wing and b) flexible wing at $\Lambda = 50$ deg.

this evidence suggests that vibrations of the leading edge are essential in the lift enhancement.

Because there are self-excited wing vibrations that accompany the lift enhancement in the poststall region, it is worth examining the effect of these vibrations on the force fluctuations. Figure 6 shows the variation of the rms lift coefficient with incidence for all the wings. The level of buffet decreases significantly with sweep angle, with peak rms values of the 60-deg wing reaching just a third of that observed over the 40-deg wing. Although there is clearly an increase in the level of buffet in the region of interest (around the stall angle), the peak rms lift coefficient is roughly equal for the flexible and rigid wings. This is important, because it signifies that the lift improvements can be achieved without the imposing high lift-force fluctuations. As it will be demonstrated later, the lift enhancement is related to the reattachment of the separated flow in the poststall region, and therefore there is no increase in the lift fluctuations. On the other hand, the fluctuations of the rolling moment are strongly affected by wing flexibility. It was shown in [16] that a significant increase in rms rolling moment was observed in the lift-enhancement region for the flexible wings and this increase was not observed for the rigid wings. This was found to be due to the vibration mode of the wing, as explained next.

For the $\Lambda = 50$- deg flexible wing, the spectral characteristics of the wingtip vibrations are summarized in Fig. 7, which shows the variation of cross-spectral amplitude and phase angle between the wingtip accelerations as a function of normalized frequency (Strouhal number, Sr) and incidence. Considering first the variation of cross-spectral amplitude, a dominant peak at $Sr = 0.7$ between $\alpha = 24$ and 30 deg should be immediately noted. Compared with this peak, other seemingly dominant frequencies are actually very small; note that the contour scale is logarithmic. Thus, in the region of enhanced lift, the wing experiences large wingtip vibrations of a coherent frequency of $Sr = 0.7$. Further, the phase map shown in Fig. 7 shows that the wingtip vibrations are out of phase at this frequency, indicating an antisymmetric mode shape. The data suggest that the wing is vibrating in the second antisymmetric mode, but from the finite element analysis already presented, one would expect this mode to occur at around $Sr = 0.8$, which is higher than the measured frequency. This is accounted for in part by the fact that the finite element analysis considered only deflection of a planar wing, whereas in reality, significant time-averaged deflections of the wingtips were observed. It was also noticed that the presence or absence of the accelerometers at wingtips cause a slight change in the measured vibration frequency (this was confirmed when another method such as LDV or hot wire is used close to the wing surface). The measured Strouhal number in the absence of the accelerometers is $Sr = 0.74$. Figure 8, which shows a visualization of the deformation of the leading edge at an instant in time, confirms the mode shape. Looking along the leading edge, one can clearly see a

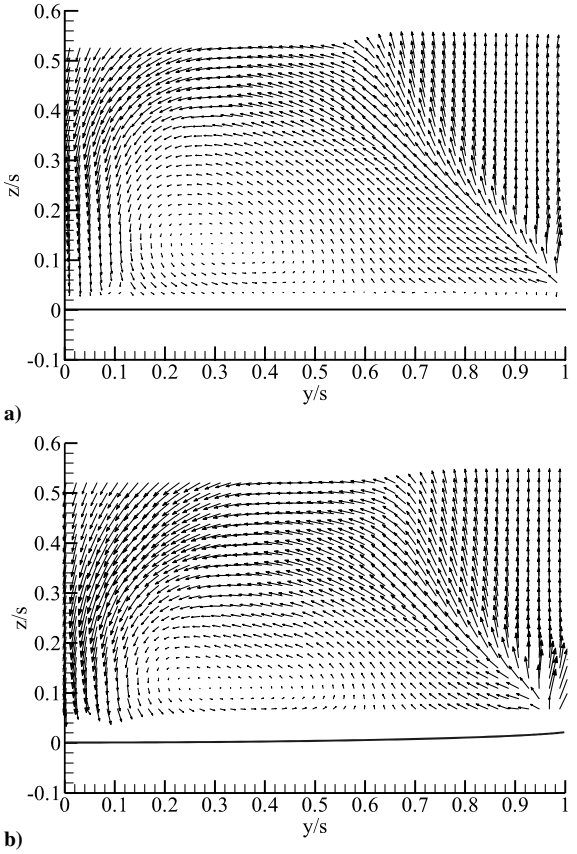

Fig. 13 Time-averaged flow in a crossflow plane at $x/c = 0.5$ for a) rigid and b) flexible delta wing at $\alpha = 25$ deg.

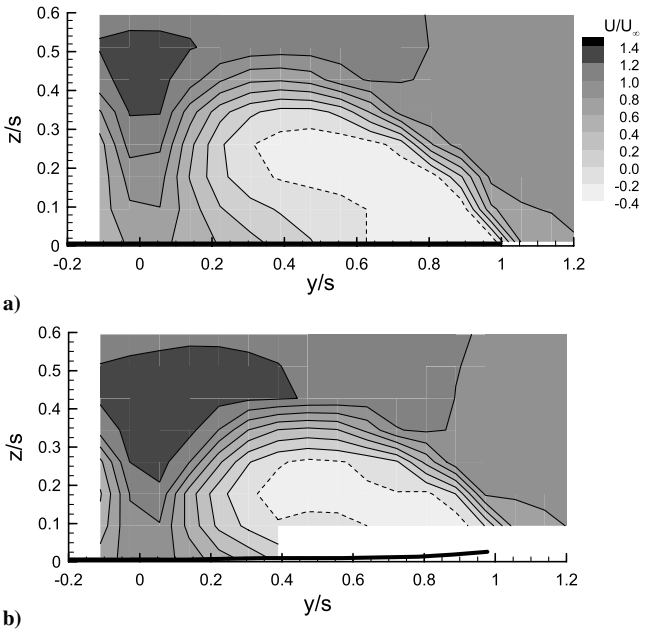

Fig. 14 Comparison of axial velocity fields measured in the crossflow plane at $x/c = 70\%$ for a) rigid and b) flexible delta wing at $\Lambda = 50$ deg and $\alpha = 25$ deg.

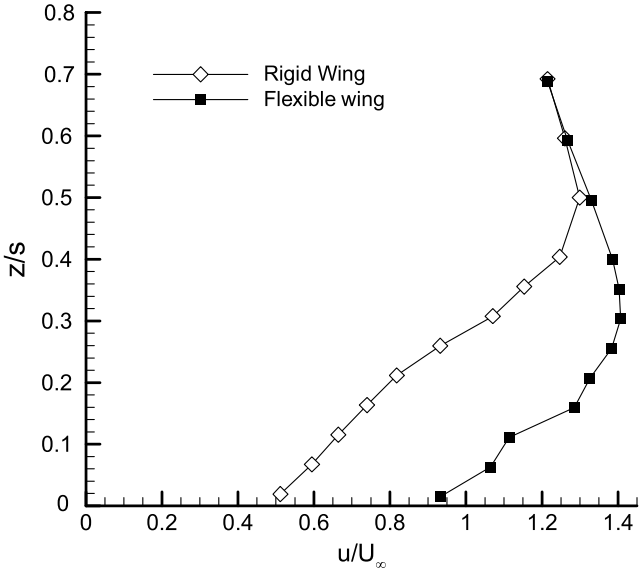

Fig. 15 Chordwise velocity profiles as a function of distance from the wing surface at $y/s = 0$ for $x/c = 0.4$; $\Lambda = 50$ deg and $\alpha = 25$ deg.

node at around three-fourths chord, as one would expect for this mode from Fig. 3. Thus, experimental evidence shows that vibration of the wing in the high-lift region is in the second antisymmetric mode.

The question as to whether an antisymmetric vibration of the wing is a necessary condition for the production of additional lift is an important one. To answer this question, experiments for a half-wing model were conducted [16]. Figure 9 shows the variation of wingtip rms acceleration with incidence for a half-wing 50-deg flexible model and compares this with the full-wing case. It is seen that the half-wing does not exhibit large self-excited vibrations in the poststall region. This suggests that antisymmetric vibration is essential for lift enhancement.

For all wings, the mode shapes and natural frequencies were predicted using the finite element analysis software ANSYS. In all cases, the mode shapes were similar to those documented for the 50-deg wing (see Fig. 3). In the experiments, lift enhancement always occurred in the second antisymmetric mode. Experimentally measured vibration frequencies are compared with the predicted frequencies of the second antisymmetric modes in Fig. 10 as a function of wing sweep angle. It is seen that there is a good agreement between the finite element prediction and the experimental results; the agreement seems to improve with increasing sweep angle (as the amplitude of the vibrations decrease). The Strouhal number for the wing vibrations are on the order of unity.

B. Flow Topology

Figure 11 shows visualizations of the surface flow at $\alpha = 27$ deg for the rigid and flexible delta wings with sweep angle $\Lambda = 50$ deg. This angle of attack is slightly lower than the stall angle of the flexible wing, which is $\alpha = 28$ deg. For the rigid wing, stalled flow is evident and large-scale unsteadiness was observed in the real-time video footage. For the flexible wing, however, a localized region of reattachment was observed near the wing centerline. Although the large regions of reversed flow are also observed toward the leading edges in this case, the flow was much less unsteady and clearly energized by the buffeting effect observed at this incidence.

To obtain quantitative information, PIV measurements of the near-surface flow were undertaken. Figure 12 shows the streamline pattern near the wing surface over the rigid and flexible wings at the same angle of attack ($\alpha = 27$ deg). It is seen that the flow over the rigid wing at this high incidence is completely stalled. The velocity magnitudes (not shown here, but discussed in [16]) indicate that the maximum velocity is around $u/U_\infty = 0.3$ in the flow-reversal region near the leading edges and that the flow toward the centerline is devoid of the high axial velocities. A pair of foci is identified in the streamline pattern of the time-averaged flow for the rigid wing. There is some asymmetry in the streamline pattern with respect to the wing centerline. The streamline pattern for the flexible wing at the same angle of attack shown in Fig. 12b demonstrates a symmetrical time-averaged flow. Significant regions of flow reversal are observed over the wing, with high negative axial velocities [16] peaking at $u/U_\infty = -0.38$. Along the centerline, high positive axial velocities are observed [16], peaking at around $u/U_\infty = 0.67$. A node exists on the centerline at around $x/c = 0.2$, and all surface streamlines on the wing issue from this node, indicating that it is a node of attachment.

Similar streamline patterns have also been observed over rigid wings of 38.7-deg leading-edge sweep [20] at $\alpha = 10$ deg and of 50-deg sweep [8] at $\alpha = 20$ deg. The similarity between the surface flow topologies between these two cases is very good, despite the very different flow conditions. However, in neither case was an attachment node recorded along the centerline, indicating that the flow around the apex does not separate and remains attached along the length of the wing. This is likely to be due to the lower incidences of these wings compared with the flexible wing being studied herein. The data show that the flow over the flexible wing is much more coherent than that over the rigid wing at the same incidence. The flexibility clearly results in substantial improvements to the flow and allows the shear layer to continue to reattach to much higher angles of attack than would otherwise be expected.

Figure 13 shows the velocity field for the time-averaged flow in a crossflow plane at $x/c = 0.5$ and $\alpha = 25$ deg for the rigid and flexible delta wings. This incidence is slightly farther away from the stall, but has strong similarities to $\alpha = 27$ deg discussed already. Only the flow over the half-wing was captured, and the solid line at $z = 0$ represents the location of the rigid wing (whereas the curved one is that of the flexible wing). It is clear from the crossflow measurements that the flow over the flexible wing appears to be more

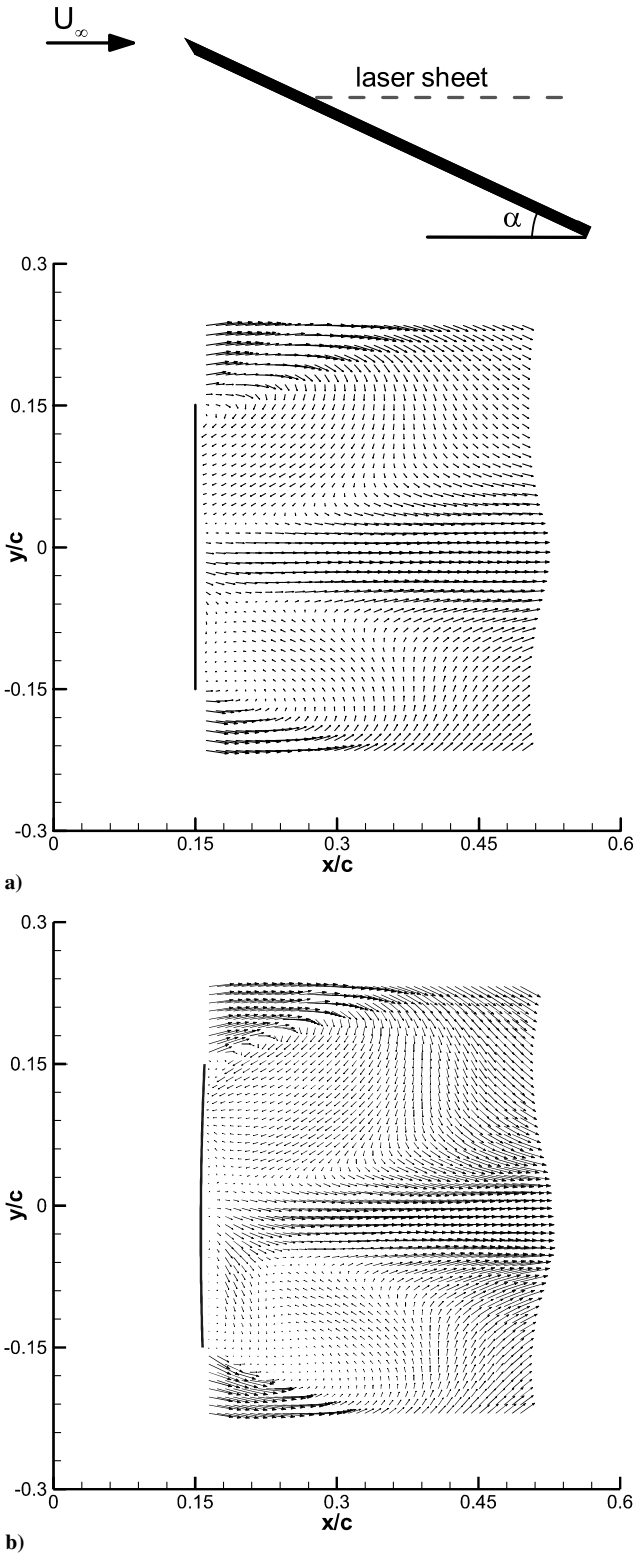

Fig. 16 Time-averaged velocity in a streamwise plane for a) rigid and b) flexible delta wing at $\alpha = 25$ deg and $x/c = 0.15$.

organized than that over the rigid wing. Moreover, a clear reattachment region is observed near the centerline for the flexible wing. Overall, there is the appearance of a stronger and more coherent vortical structure for the flexible wing. The vertical extent or size of the vortical flow is smaller for the flexible wing.

Of course, the two-dimensional PIV measurements in a crossflow plane shown here do not provide any information on whether there is any axial flow in the vortical flow regions on the rigid and flexible wings. For the rigid wing, it is not expected that there will be any axial velocity because the flow is completely stalled for these incidences. However, with the reattachment of the flow for the flexible wing, it is not known whether axial flow develops in the cores of the vortices. To clarify this, LDV measurements were performed. Figure 14 shows the results of LDV measurements of the chordwise velocity field in the crossflow plane at $x/c = 0.7$ for the rigid and flexible 50-deg wings at $\alpha = 25$ deg. It is seen that there is no evidence of axial flow forming within the reattached region. For the rigid wing, the data show a large region of reversed flow extending well above the surface of the wing, but a region of high axial velocity remains along the centerline, albeit at a considerable distance from the wing surface. The chordwise velocity field over the flexible wing shares many similarities with that of the rigid wing. Again, a region of reversed flow extending well above the wing surface is evident along with a region of high axial velocity above the surface near the centerline. However, the region of flow reversal is reduced in extent and appears flatter than that for the rigid wing, whereas the region of high axial velocity above the centerline is larger and extends closer to the wing surface. Figure 15 shows the axial velocity profiles measured above the centerline of the rigid and flexible 50-deg wings at $x/c = 0.4$. For both cases, the flexible wings exhibit much higher axial velocities toward the wing surface than the rigid wings, whereas further away from the wing, the velocity profiles merge.

To understand the features of the reattachment process and also to obtain time-accurate data, further measurements with the high frame-rate PIV system were performed. The inset in Fig. 16 shows the laser sheet that was set parallel to the freestream, and the camera was placed orthogonal to it. Although flow in several planes was studied in detail, a particular one, which was at $x/c = 0.15$, will be discussed here. Figure 16 shows the mean flow results for the rigid (top image) and flexible (bottom image) delta wing at $\alpha = 25$ deg. For the rigid wing, a straight-line set at $x/c = 0.15$ represents the wing, whereas for the flexible wing, a slightly curved line represents the flexible wing. A distinct difference can be observed between the two flowfields, in which the flexible wing presents a very well-organized flow. Near the centerline ($y = 0$), there is a clear reattachment region for the flexible wing. Of course, the flow pattern in this streamwise plane is different from that in a crossflow plane. The flow moves away from the wing near the centerline, and increasing velocity magnitude is indicative of the reattachment near the centerline. Contrary to the results for $\alpha = 27$ deg discussed earlier, the flow near the apex already shows the attachment for $\alpha = 25$ deg. Some spectral features of such measurements will be discussed in the next section.

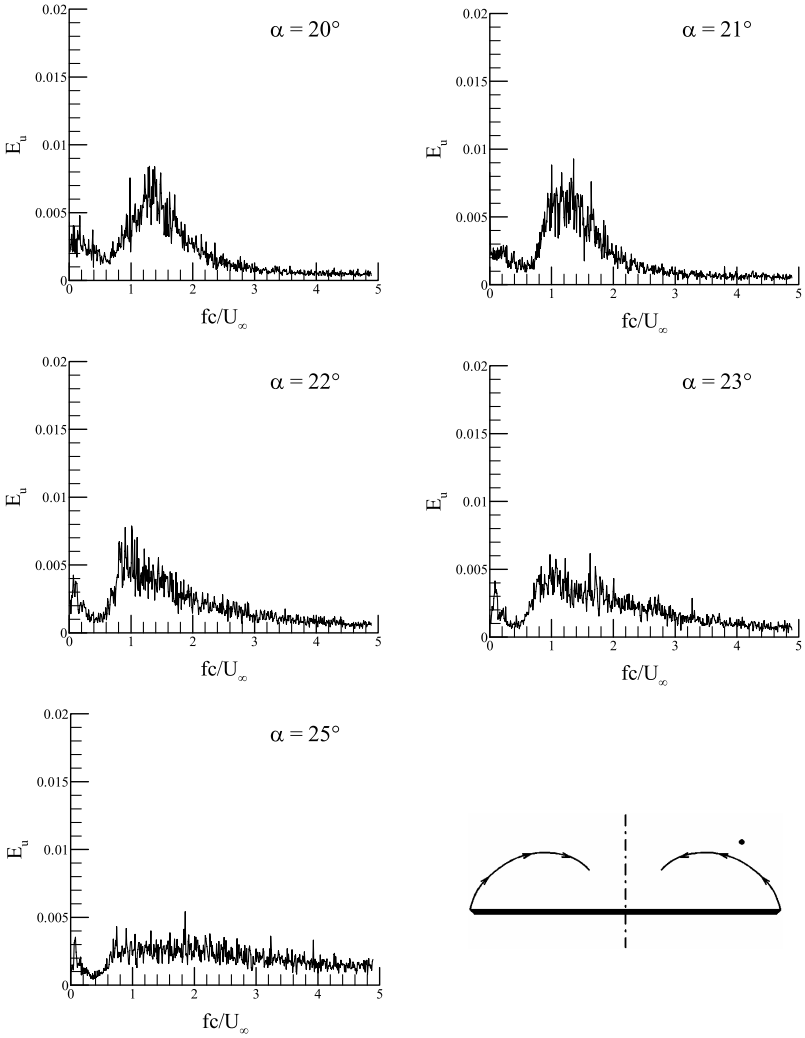

Fig. 17 Effect of angle of attack on the spectra of velocity fluctuations for $\Lambda = 50$-deg rigid wing at $x/c = 0.7, y/s = 0.75$, and $z/s = 0.44$; the schematic shows the measurement location.

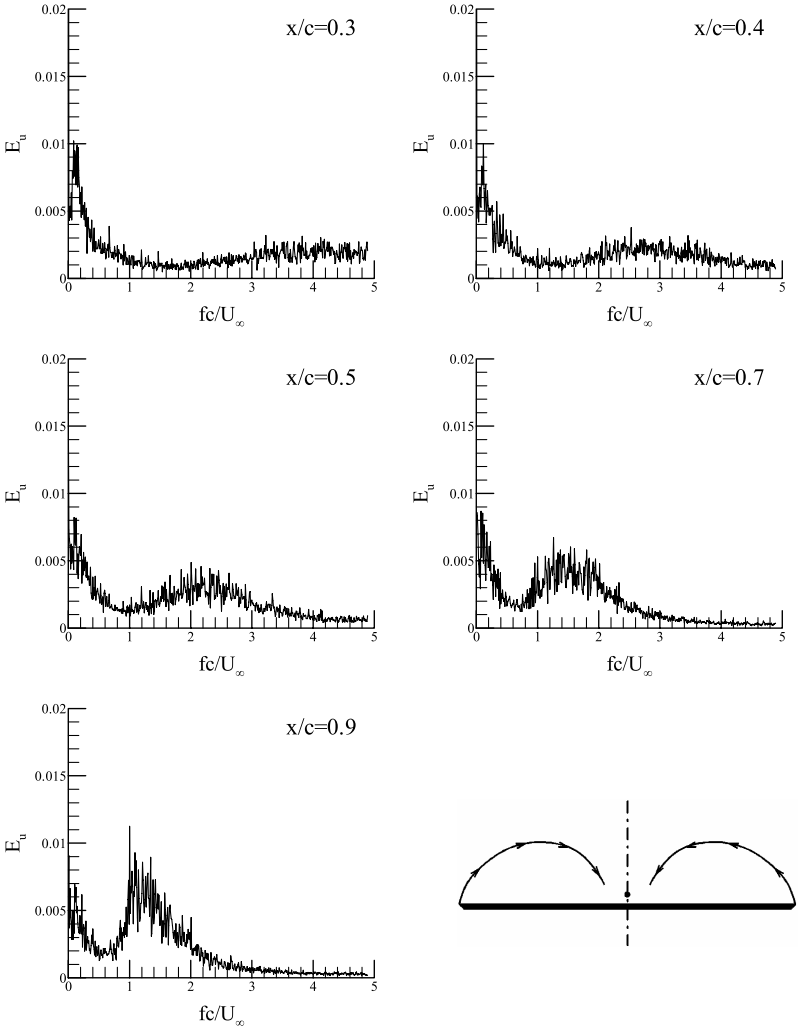

Fig. 18 Effect of streamwise location on the spectra of velocity fluctuations for a $\Lambda = 50$-deg rigid wing at $\alpha = 20$ deg, $y/s = 0$, and $z/s = 0.06$; the schematic shows the measurement location at the wing centerline.

C. Spectral Characteristics

Hot-wire measurements were conducted for spectral analysis of unsteady flow features. These measurements were taken with a single hot wire and also with two hot wires (for simultaneous measurements). Figure 17 shows the spectra of the velocity fluctuations at $x/c = 0.7$, $y/s = 0.75$, and $z/s = 0.44$ for various angles of attack in the range of $\alpha = 20$ to 25 deg for the $\Lambda = 50$-deg rigid wing. The dominant peaks are seen in all cases in the poststall region. Note that for $\alpha = 20$ deg, vortex breakdown is already at the apex of the wing. It is seen that a broad peak exists in the spectra for this and higher angles of attack in the poststall region, and the center frequency of the peaks is in the range of $Sr = 1$ to 2. Because the location of measurements is close to the separated shear layer, it is believed that these peaks correspond to the dominant frequency of the shear-layer structures. As discussed already, the dominant frequency of structural vibration was around $Sr = 0.74$, which compares well with the dominant frequencies detected over the rigid wings [7,8,21]. All these values of Strouhal numbers are much smaller than the frequency of the Kelvin–Helmholtz instability for slender delta wings [22]. In fact, they are closer to the frequency of the helical mode instability of vortex breakdown. However, in the poststall region ($\alpha \geq 20$ deg), there is no breakdown. Hence, it is believed that these are due to the shear-layer instabilities.

Figure 18 shows the effect of streamwise distance on the spectra of velocity fluctuations for $\alpha = 20$ deg. It is seen that the center peaks detected at the wing centerline ($y/s = 0$) decrease with increasing streamwise distance. The center peaks vary from $Sr = 4$ to 1, with streamwise distance changing from $x/c = 0.3$ to 0.9. This is not surprising and is very similar to the variation of dominant frequencies with streamwise distance for slender delta wings [3]. The shear-layer structures shed in a conical way, which results in the dominant frequencies decreasing with streamwise distance.

For the flexible wing at $\alpha = 25$ deg, the measurements of the coherence [18] between the two velocity signals at two locations, which are the mirror images, confirmed the antisymmetric nature of the oscillations. Because the antisymmetric vibrations and modal shapes were observed for the flexible wing, vortex (or shear-layer) interactions were suspected for the rigid wing. To investigate this possibility, simultaneous measurements of velocity fluctuations at two locations, which are the mirror images, were conducted. These measurements indicated that there was no coherence between the two signals, as shown in Fig. 19 for $\alpha = 15$ deg (prestall), 20 deg (stall), and 25 deg (poststall) for the rigid wing. This was somewhat surprising in that the dominant peaks observed in the spectra are not correlated at all for the rigid wing in both the prestall and poststall regimes. The origin of the wing vibrations in the poststall region might not be a fluid dynamics phenomenon, but rather a structural response to the unsteady flow.

Similar experiments were carried out for the flexible delta wing. Spectra of velocity fluctuations along the shear layer for $\alpha = 25$ deg at $x/c = 0.7$ are shown in Fig. 20. The measurement locations are varied from $y/s = 1$ to 0.5 along the shear layer. The large sharp peak in each spectrum corresponds to the wing vibrations. It is interesting that near the leading edge ($y/s = 1$), there is also a broad peak centered around $Sr \approx 5$. This broad peak presumably corresponds to the natural frequency of the shear-layer instability. The center

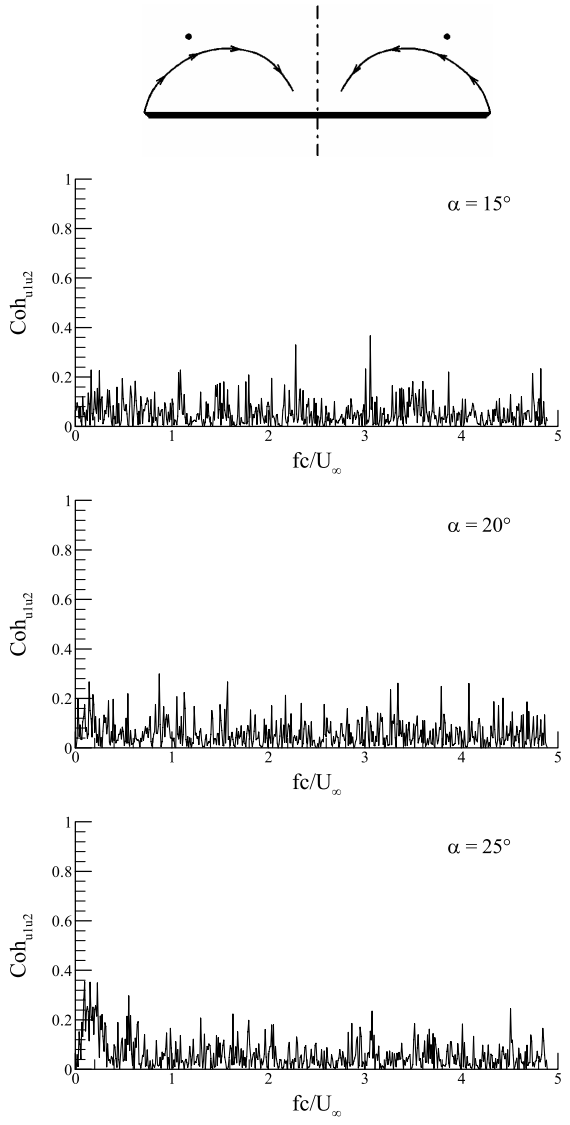

Fig. 19 Coherence between the two velocity signals for $\Lambda = 50$-deg rigid wing at $x/c = 0.7$, $y/s = \pm 0.75$, and $z/s = 0.44$; the schematic shows the locations of the hot-wire probes.

frequency of the broad peak decreases as the measurement location is moved inboard along the shear layer. This is likely to be due to the vortex merging process. By the time the midspan ($y/s = 0.5$) is reached, the broad peak is around $Sr \approx 1$ and coincident with the frequency of the wing vibrations.

In summary, the hot-wire measurements showed that there are dominant peaks in the spectra of velocity fluctuations in the range of $Sr \approx 1$ to 5 over a range of incidences. These correspond to the shear-layer instabilities, and their values depend on both spanwise and streamwise location as the three-dimensional vortical structures evolve and merge. Although these dominant peaks are in the same range as the optimum frequencies observed for the flexible delta wings, the effect of excitation is significantly more complicated than for quasi-2D shear layers. The main mechanism for lift enhancement seems to be related to the excitation of the shear-layer instabilities. The self-induced vibrations of the wing energize the vortices shed into the shear layer and promote reattachment to the wing surface, resulting in delayed stall and increased lift. This is similar to the response of the flow over a backward-facing step to the periodic excitation. It is well known that for both laminar and turbulent separation [23], excitation enhances the formation of vortical structures and substantially reduces reattachment length. Effect of excitation of the shear layer on delta wings was also investigated previously [24–26]. Gad-el-Hak and Blackwelder [24] studied the effect of periodic tangential blowing along the leading edge of a 60-deg delta wing. The results showed that by blowing at a frequency of approximately half the natural shedding frequency, the crossflow structure of the primary vortex could be made more organized. Benefits of shear-layer excitation are not restricted to the use of leading-edge blowing, as shown by Cipolla and Rockwell [25], who studied the effect of a periodic pitching oscillation on a stalled 45-deg wing. For pitching frequencies in the range of $0.5 < Sr < 1.0$, the extent of the stall region was decreased compared with the stationary wing. Perhaps the most relevant study was conducted by Margalit et al. [26], who investigated the use of synthetic-jet technology applied along the leading edges of a 60-deg delta wing. Significantly, lift enhancements of around 15% were exhibited for forcing frequencies in the range of $1.0 < Sr < 4.0$. Further, these lift enhancements were observed in the poststall region between $\alpha = 35$ and 40 deg.

An interesting aspect of the reattachment near the wing centerline for the flexible wings is that the unsteady flow exhibits fluctuations in the antisymmetric mode as found by the high-frame-rate PIV measurements (with a data rate of 1.5 kHz) in this investigation. The spectral analysis was performed for the PIV measurements in a streamwise plane (see the inset in Fig. 16 for the orientation of the plane) at $x/c = 0.5$. In Fig. 21a, the time-averaged flow for the flexible wing is presented along with the points at which spectral analysis was performed. Note that the flowfield is the result of two different captures over the wing surface, hence the gap between the two flowfields. These two points were chosen because they are in the reattachment region near the wing centerline. The cross-spectral density was calculated for the two points across the shear layer near the centerline of the flexible wing and is shown in Fig. 21b. The largest peak corresponds to the frequency of the wing vibrations, and the two signals were out of phase because the phase angle between the two points is near 180 deg (not shown here). It is interesting that antisymmetric vortical flows were observed [22] in various previous experiments when the vortex breakdown was over the wing: antisymmetric motion of vortex breakdowns, antisymmetric pressure fluctuations, and antisymmetric wingtip accelerations for a slightly flexible delta wing. It has been suggested [22] that a crossflow instability, for which the unsteady flow is antisymmetric, may arise from a loss of stability by the symmetric mean flow. There is evidence [27] of existence of the crossflow instability. However, in the present experiments in the poststall region, we found no evidence of such interactions for the rigid wing. Further research is needed to understand the origin of the antisymmetric wing vibrations and whether there is any relation to a fluid dynamic phenomenon.

D. Water-Tunnel Experiments

Experiments in the water tunnel allowed us to explore the reattachment of the separated flow for more flexible wings. Flow visualizations for a rigid and various flexible wings are shown in Fig. 22 for $\alpha = 20$ deg and $\Lambda = 50$ deg. Here, the flexibility parameter λ_s is varied in a wider range (note that the flexible wing in the wind-tunnel experiments had a $\lambda_s = 3.1$). It is seen in Fig. 22 that the dye-free region near the wing centerline is much broader for the flexible wings, indicating earlier reattachment of the separated flow. For the most flexible wing ($\lambda_s = 21.3$), it is interesting that reformation of the leading-edge vortex and rapid breakdown are visible in a region very close to the wing apex. Hence, with increasing flexibility, there is evidence of a change in the structure of the flow and axial flow develops within the reattached region. This is somewhat unexpected in that the flexibility not only promotes earlier reattachment but also helps reformation of the leading-edge vortices.

Figure 23 shows the vectors and contours of magnitude of time-averaged velocity in a crossflow plane at $x/c = 0.80$ for rigid and flexible wings for an even larger incidence of $\alpha = 25$ deg. For the rigid wing, there is no reattachment, however, for the flexible

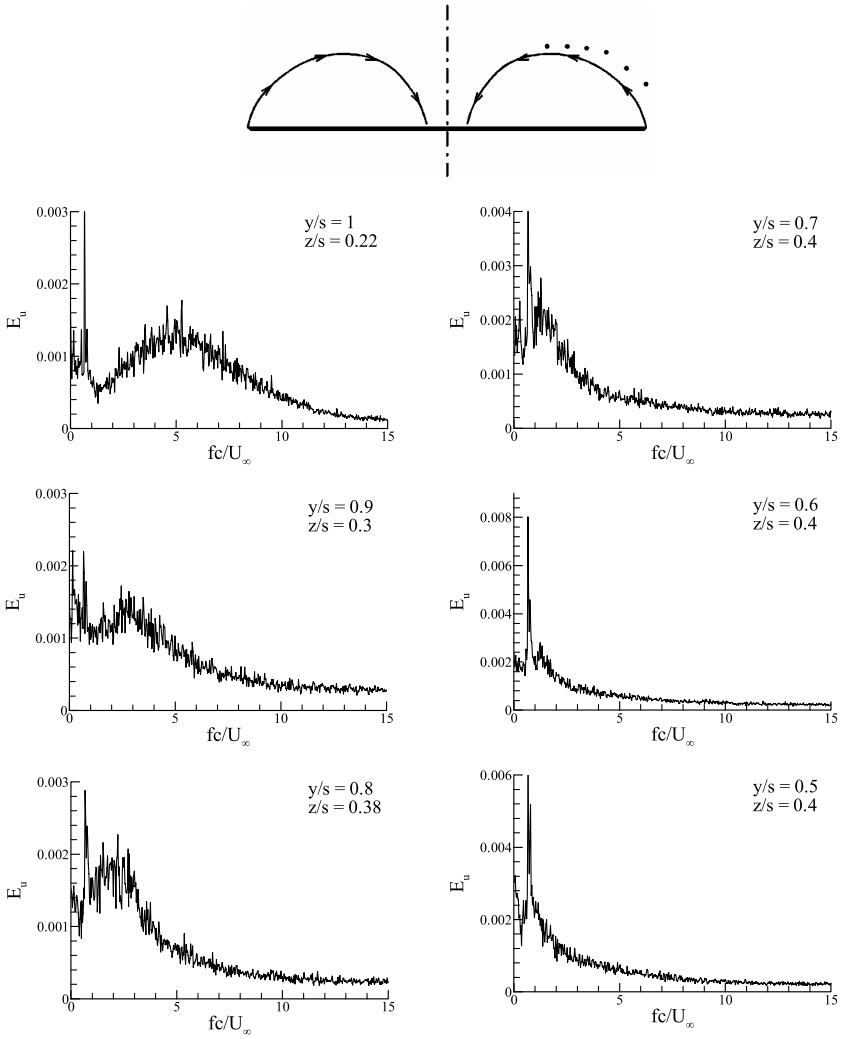

Fig. 20 Spectrum of velocity fluctuations along the shear layer for $\Lambda = 50$-deg flexible wing for $\alpha = 25$ deg at $x/c = 0.7$; the schematic shows the measurement locations.

wings, there is larger velocity near the wing centerline and reattachment in the time-averaged sense. The vorticity distributions [17] (not shown here) reveal that there are substantial effects on the vortical flow with increasing wing flexibility, because the oscillating leading edge is an unsteady source of vorticity. In fact, the time-averaged vorticity flux is expected to increase with the vibrations of the leading-edge, because this term is proportional to $\bar{U}_s^2$, where U_s denotes the velocity outside the boundary layer at the separation point. This is confirmed by the larger values of vorticity for the flexible wings [17]. The variation of circulation with the spanwise bending stiffness normalized by freestream dynamic pressure, λ_s, is shown in Fig. 24. It is seen that the circulation of the vortical flow in a crossflow plane increases with flexibility in comparison with the rigid wing.

IV. Conclusions

Passive lift enhancement for flexible nonslender delta wings was demonstrated as a potential method for the control of vortex-dominated wing flows. Over the range of sweep angles tested, the greatest lift enhancement was observed over the wing with the lowest leading-edge sweep angle, whereas for the only slender wing ($\Lambda = 60$ deg) considered, no lift enhancement was observed. Lift enhancement was achieved in the poststall region and increased the lift coefficient by more than 50% and delayed stall by up to 7 deg for the $\Lambda = 40$-deg wing. Large time-averaged structural deflections and vibrations accompany this behavior, along with a switching of the dominant mode of vibration from the first mode to the second antisymmetric mode. Although there is significant time-averaged deflection of the wing, particularly at high incidences, this does not contribute to the lift-enhancement phenomenon. Wingtip acceleration measurements for full-wing and half-wing 50-deg models showed that the half-wing model did not experience self-excited vibrations, which suggests that the antisymmetric vibration is a necessary condition for the lift enhancement to occur. The generation of self-induced antisymmetric vibrations of leading edges is not completely understood, however, it is certain that these vibrations produce the observed lift enhancement. The main mechanism of lift enhancement is the excitation of shear-layer instabilities and promotion of reattachment of the separated flow.

It was shown for the rigid wing that there are dominant peaks in the spectra of velocity fluctuations in the range of $Sr = 1$ to 5 over a range of incidences, and these correspond to the shear-layer instabilities. The center frequency of these peaks decreases with streamwise distance because the shear-layer vortices shed conically. There is also a decrease in the spanwise direction due to the vortex merging process. The Strouhal number of the dominant frequency of structural vibration was on the order of unity for all nonslender

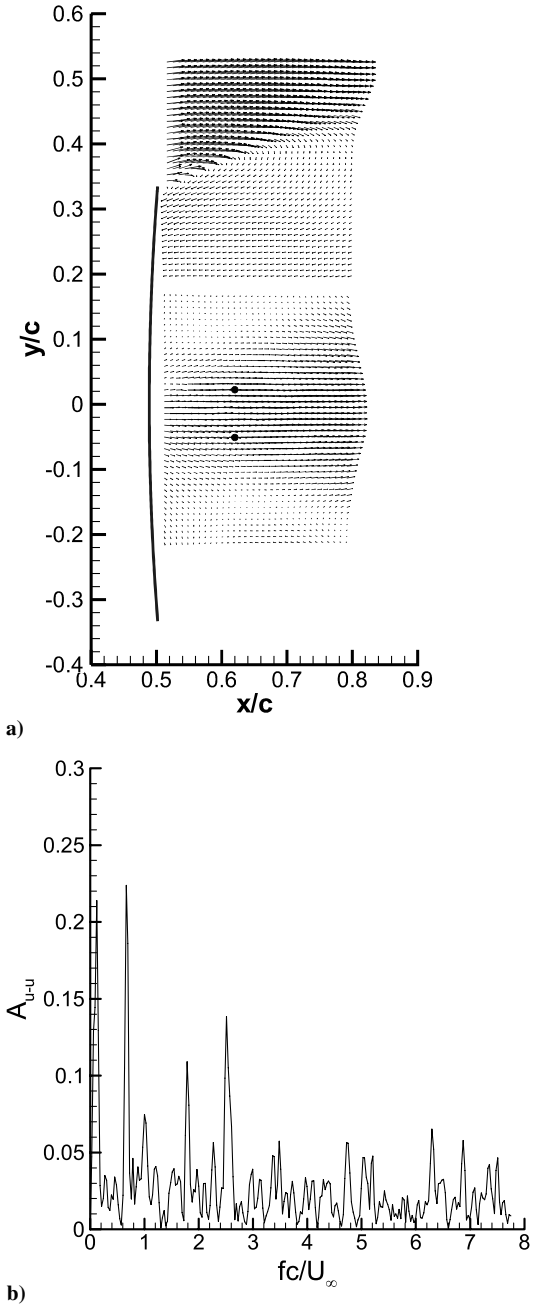

Fig. 21 High-frame-rate PIV measurements of a) time-averaged velocity in a streamwise plane at $x/c = 0.5$ for the flexible wing and (b) amplitude of the cross-spectral density of velocity fluctuations measured at two points shown in Fig. 21a for $\alpha = 25$ deg.

wings. It is proposed that vibration of the wing increases the energy of the vortices shed into the shear layer, which allows the transfer of momentum from the freestream onto the suction surface of the wing, delaying stall and allowing lift coefficient to increase.

PIV and LDV measurements demonstrated the striking difference between the flows over the flexible and rigid wings in the poststall region. The flow over the rigid wing is completely stalled in the poststall region. The effect of flexibility is to reduce the extent to the region of flow reversal that occurs over the wing surface and to promote the reattachment of the shear layer. Depending on the angle of attack, flow reattachment near or downstream of the apex is observed for the flexible wing. Although the reattachment along the wing centerline in the poststall region (of the rigid wing) produces the lift enhancement for the flexible wing, there is no axial flow forming within the reattached region in the wind-tunnel experiments. The structure of the reattached flow is similar to a three-dimensional conical separation bubble in the time-averaged sense. With

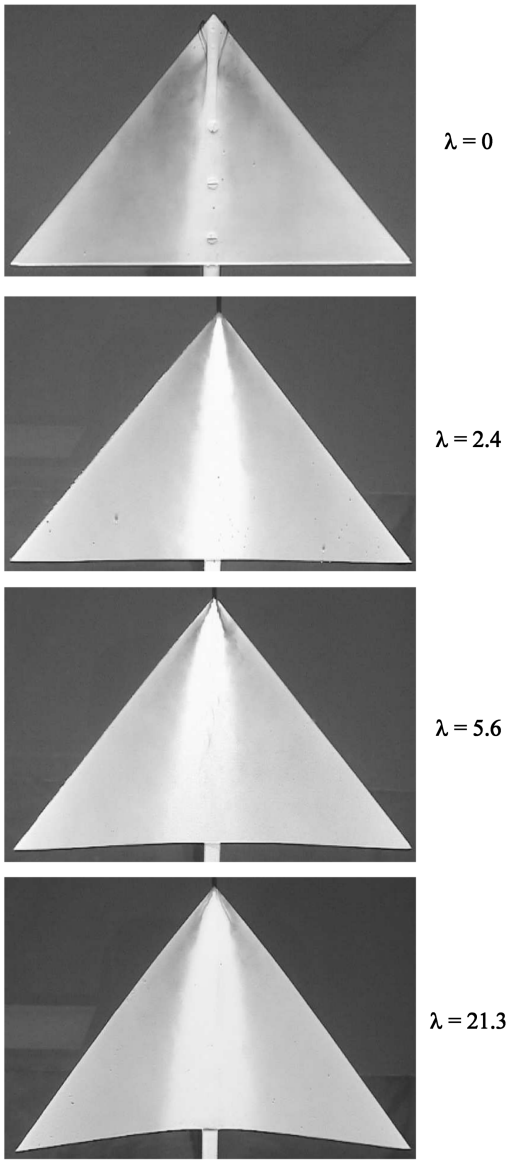

Fig. 22 Flow visualization for rigid and flexible wings in a water tunnel for $\alpha = 20$ deg.

increasing flexibility, there is evidence of axial flow developing within the reattached region in the water-tunnel experiments. There are substantial effects on the vortical flow with increasing wing flexibility, because the oscillating leading edge is an unsteady source of vorticity. The time-averaged vorticity flux increases due to the oscillating leading edge, which leads to increased circulation.

A major benefit of using wing flexibility to enhance lift in this manner is that flow control of this form is entirely passive, requiring no input of energy into the system, unlike the forms of active control discussed already. This may allow control of aircraft using this feature at much lower speeds and may have applications for aircraft that require maneuverability or simply lower landing speeds. However, there are clear disadvantages to this behavior also, such as the significant fatigue cycles through which the wing must operate.

Acknowledgments

This work is supported by the European Office of Aerospace Research and Development, U.S. Air Force Office of Scientific Research, and U.S. Air Force Research Laboratory under contract no. F61775-02-C4024. The authors would like to acknowledge additional support from the Engineering and Physical Sciences Research Council (EPSRC) Academic Fellowship in Unmanned Air Vehicles and the EPSRC grant EP/C015258/1.

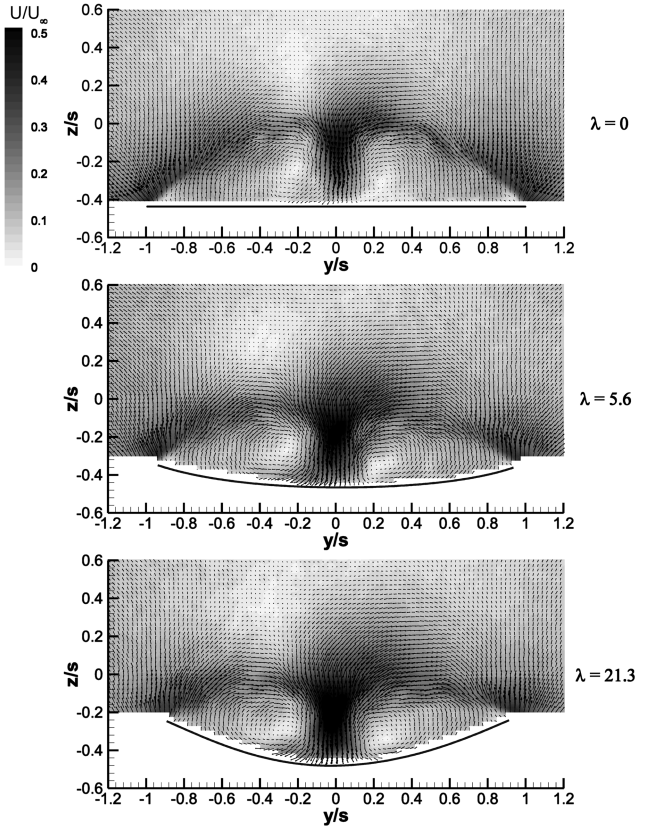

Fig. 23 Vectors and contours of magnitude of time-averaged velocity in a crossflow plane at $x/c = 0.8$ for rigid and flexible wings in water-tunnel experiments for $\alpha = 25$ deg.

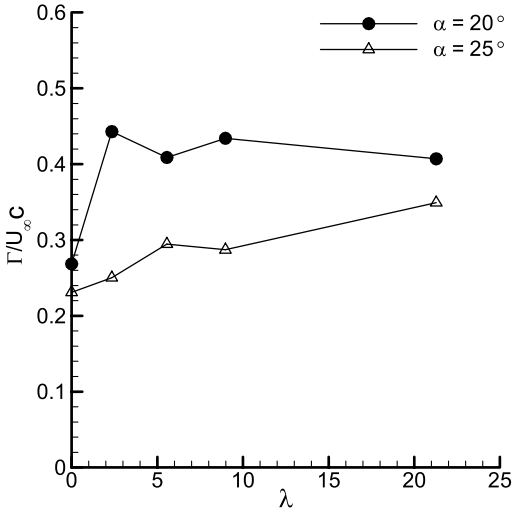

Fig. 24 Variation of normalized circulation with wing flexibility.

References

[1] Gursul, I., "Vortex Flows on UAVs: Issues and Challenges," *The Aeronautical Journal*, Vol. 108, No. 1090, Dec. 2004, pp. 597–610.

[2] Rockwell, D., "Three-Dimensional Flow Structure on Delta Wings at High Angle-of-Attack: Experimental Concepts and Issues," 31st AIAA Aerospace Sciences Meeting and Exhibit, Reno, NV, AIAA Paper 93-0050, Jan. 1993.

[3] Visbal, M. R., "Computational and Physical Aspects of Vortex Breakdown on Delta Wings," 33rd AIAA Aerospace Sciences Meeting and Exhibit, Reno, NV, AIAA Paper 95-0585, Jan. 1995.

[4] Delery, J. M., "Aspects of Vortex Breakdown," *Progress in Aerospace Sciences*, Vol. 30, No. 1, 1994, pp. 1–59.

[5] Délery, J. M., "Physics of Vortical Flows," *Journal of Aircraft*, Vol. 29, No. 5, 1992, pp. 856–876.

[6] Yaniktepe, B., and Rockwell, D., "Flow Structure on a Delta Wing of Low Sweep Angle," *AIAA Journal*, Vol. 42, No. 3, Mar. 2004, pp. 513–523.

[7] Gursul, I., Gordnier, R., and Visbal, M., "Unsteady Aerodynamics of Nonslender Delta Wings," *Progress in Aerospace Sciences*, Vol. 41, No. 7, 2005, pp. 515–557.

[8] Taylor, G., and Gursul, I., "Buffeting Flows over a Low Sweep Delta Wing," *AIAA Journal*, Vol. 42, No. 9, Sept. 2004, pp. 1737–1745.

[9] Earnshaw, P. B., and Lawford, J. A., "Low-Speed Wind-Tunnel Experiments on a Series of Sharp-Edged Delta Wings," Aeronautical Research Council, Reports and Memoranda No. 3424, Mar. 1964.

[10] Wentz, W. H., and Kohlman, D. L., "Vortex Breakdown on Slender Sharp-Edged Wings," *Journal of Aircraft*, Vol. 8, No. 3, Mar. 1971, pp. 156–161.

[11] Lee, M., and Ho, C., "Lift Force of Delta Wings," *Applied Mechanics Reviews*, Vol. 43, No. 9, 1990, pp. 209–221.

[12] Polhamus, E. C., "Predictions of Vortex-Lift Characteristics by a Leading-Edge Suction Analogy," *Journal of Aircraft*, Vol. 8, No. 4, Apr. 1971, pp. 193–199.

[13] Gray, J., Gursul, I., and Butler, R., "Aeroelastic Response of a Flexible Delta Wing Due to Unsteady Vortex Flows," 41st Aerospace Sciences Meeting and Exhibit, Reno, NV, AIAA Paper 2003-1106, Jan. 2003.

[14] Gordnier, R., and Visbal, M. R., "Computation of the Aeroelastic Response of a Flexible Delta Wing at High Angles of Attack," *Journal of Fluids and Structures*, Vol. 19, No. 6, July 2004, pp. 785–800.

[15] Taylor, G. S., and Gursul, I., "Lift Enhancement over a Flexible Low Sweep Delta Wing," 2nd AIAA Flow Control Conference, Portland, OR, AIAA Paper 2004-2618, 2004.

[16] Taylor, G. S., Kroker, A., and Gursul, I., "Passive Flow Control over Flexible Nonslender Delta Wings," 43rd Aerospace Sciences Meeting and Exhibit, Reno, NV, AIAA Paper 2005-0865, Jan. 2005.

[17] Vardaki, E., Gursul, I., and Taylor, G., "Physical Mechanisms of Lift Enhancement for Flexible Delta Wings," 43rd Aerospace Sciences Meeting and Exhibit, Reno, NV, AIAA Paper 2005-0867, Jan. 2005.

[18] Gursul, I., Vardaki, E., and Wang, Z., "Active and Passive Control of Reattachment on Various Low-Sweep Wings," 44th AIAA Aerospace Sciences Meeting and Exhibit, Reno, NV, AIAA Paper 2006-506, Jan. 2006.

[19] Gursul, I., Vardaki, E., and Taylor, G., "Flow Control with Wing Flexibility," *1st European Forum on Flow Control*, Univ. of Poitiers, Poitiers, France, Oct. 2004, pp. 41–43.

[20] Yavuz, M. M., Elkhoury, M., and Rockwell, D., "Near-Surface Topology and Flow Structure on a Delta Wing," *AIAA Journal*, Vol. 42, No. 2, 2004, pp. 332–340.

[21] Gordnier, R. E., and Visbal, M. R., "Compact Differences Scheme Applied to Simulation of Low-Sweep Delta Wing Flow," *AIAA Journal*, Vol. 43, No. 8, Aug. 2005, pp. 1744–1752.

[22] Gursul, I., "Review of Unsteady Vortex Flows over Slender Delta Wings," *Journal of Aircraft*, Vol. 42, No. 2, Mar.–Apr. 2005, pp. 299–319.

[23] Roos, F. W., and Kegelman, J. T., "Control of Coherent Structures in Reattaching Laminar and Turbulent Shear Layers," *AIAA Journal*, Vol. 24, No. 12, Dec. 1986, pp. 1956–1963.

[24] Gad-el-Hak, M., and Blackwelder, R. F., "Control of the Discrete Vortices from a Delta Wing," *AIAA Journal*, Vol. 25, No. 8, 1987, pp. 1042–1049.

[25] Cipolla, K. M., and Rockwell, D., "Flow Structure on Stalled Delta Wing Subjected to Small Amplitude Pitching Oscillations," *AIAA Journal*, Vol. 33, No. 7, July 1995, pp. 1256–1262.

[26] Margalit, S., Greenblatt, D., Seifert, A., and Wygnanski, I., "Active Flow Control of a Delta Wing at High Incidence Using Segmented Piezoelectric Actuators," 1st AIAA Flow Control Conference, St. Louis, MO, AIAA Paper 2002-3270, June 2002.

[27] Lee, Y. L., and Gursul, I., "An Investigation of Unsteady Interactions of a Vortex Pair over Delta Wings," 41st Aerospace Sciences Meeting and Exhibit, Reno, NV, AIAA Paper 2003-423, Jan. 2003.

F. Coton
Associate Editor